Electronic Supplementary Material (ESI) for ChemComm.
This journal is © The Royal Society of Chemistry 2022

Customizable Assembly of Free-standing Integrated Electronics for Wearables by Phase Separation

Hongting Ma,†[a] Chuanrui Chen,†[a] Peihao Cheng,[a] Kaizhou Yang,[a] Xiaodong Geng,[a] Junlin Ma,[a] Fengjuan Lv,[a] Yue Jiang,[a] Quanli Liu,[a] Yan Su,[b] Jian Li,[c] and Nan Zhu[a]*

†These authors contributed equally

[a]Zhang Dayu School of Chemistry, Dalian University of Technology, Dalian, Liaoning, 116024, China E-mail: nanzhu@dlut.edu.cn

[b]School of Chemical Engineering, Dalian University of Technology, Dalian, Liaoning, 116024, China

[c]Center for Reproductive Medicine, Dalian Women and Children's Medical Center (Group), Dalian, China

1. Experimental Section

Synthesis of graphene oxide (GO). GO was prepared by modified Hummer method.[1] Firstly, 2.5 g $K_2S_2O_4$ and 2.5 g P_2O_5 were added in 7.5 ml H_2SO_4 and the mixture was heated to 80 °C. Secondly, 5.0 g natural graphite was added into the mixing solution under continuous stirring for 3 h and then cooled for 6 h. Distilled water was used to wash the mixture until pH up to 7, and black solid mixture was collected after drying overnight. Thirdly, 1.0 g of above mixture and 3.0 g $KMnO_4$ were carefully added in 23 ml H_2SO_4 under stirring in an ice-water bath. After that, mixture was transferred into a round-bottomed flask and stirred at 35 °C. After 2 h reaction, 180 ml distilled water was added for another 15 min stirring followed with 2.5 ml H_2O_2 (30%). Finally, mixture was washed with 250 ml HCl solution (0.1 wt.%), and yellow GO suspension was received after centrifuged.

Preparation of Pt@Au_{to}/rGO. The preparation of Pt@Au_{to}/rGO was through two steps. Au/rGO was synthesized as first step according to previous reports.[2] Briefly, 100 mg GO was dispersed in 20 mL PD solution by ultrasound for 10 min, and then 87 µL $AgNO_3$ (1g L^{-1} in PD solution) was introduced in the mixture. After heating to 200 °C, 6.0 mL 1,5-pentanediol (PD) contained 1.5 g poly(vinyl pyrrolidone) (PVP) and 1.24 mL of 10 wt.% $HAuCl_4 \cdot 4H_2O$ in 4 mL PD solution were alternatively added into mixture for 7 min. The resulting solution was further stirred and refluxed for 1 h. After cooling to room temperature, Au/rGO NPs were separated by centrifugation at 10000 rpm for 15 min. Ethanol was used to wash products for several times to remove excess PVP. Final products were dried in vacuum oven at 60 °C.

Later, prepared Au rGO NPs was dispersed in 11 mL distilled water and heated to 50 °C under stirring. After that, 950 µL of 20wt.% H_2PtCl_6 and 0.2432 g L-ascorbic acid (AA) in 7 mL distilled water were added to mixture for another 14 h standing reaction.[2] Electrochemical catalysis of Pt@Au_{to}/rGO was finally received by centrifugation at 10000 rpm for 15 min after being washed by distilled water for three times.

Preparation of nitrogen-doped carbon network materials (N-C_{net}). Electrocatalysts of N-C_{net} material for ORR was synthesized by three steps.[3] Firstly, urea was heated to 550 °C in a crucible for 4 h and cooled to room temperature to get light yellow (graphitic carbon nitride) g-C_3N_4 power. Secondly, 1 g of above g-C_3N_4 was dispersed in 40 mL distilled water with 0.3 M dopamine hydrochloride (DA) and ultrasonicated for 2 h. The mixture was then heated to 120 °C in an autoclave for 10 h. g-C_3N_4@PDA was received after being washed by distilled water and dried at 80 °C overnight. Finally, g-C_3N_4@PDA was heated in nitrogen to 900 °C for 2 h and then cooled to room temperature for obtaining N-C_{net} materials.

Preparation of $NiCo_2O_4$ NPs. Nanowire structure of $NiCo_2O_4$ materials were fabricated as previous report.[4] Briefly, 60 mL mixed solution of ethanol/deionized water (with equal volume), consisting of 1.16 g of $Co(NO_3)_2 \cdot 6H_2O$, 0.58 g of $Ni(NO_3)_2 \cdot 6H_2O$, and 1.44 g of urea were transferred to 100 mL Teflon-lined stainless-steel autoclave lines. The mixture was heated to 100 °C for 8 h and then cooled down to room temperature. The mixture was washed by deionized water for several times and then dried in air at 60 °C. Well defined crystallized $NiCo_2O_4$ NPs were obtained by heating above products to 300 °C in air for 2 h.

Preparation of KOH-PVA hydrogel electrolyte. Solid electrolyte was synthesized by dissolving 6 g PVA in 40 ml distilled water at 85 °C for 2 h. After PVA was totally dissolved, 20 ml KOH solution (3 M) was added under continuously stirring for another 30 min. At last, the solution was poured into plastic mold with 1 mm thickness, freezing at -15 °C for 6 h and thawing at room temperature for 2 h to obtain physical cross-liking PVA chain and keep viscosity.

Fabrication of the motion sensor. The motion sensor was achieved by vapor phase polymerization method. Briefly, a piece of polyurethane sponge was immersed in 50 mL $FeCl_3$ solution (0.1 M). After sucking enough solution, the sponge was dried at 60 °C for 1 h, and the process was repeated for three times. As prepared sponge was further exposed to pyrrole (Py) monomers in a closed chamber for 30 min. Pyrrole monomers reacted with the oxidant of $FeCl_3$, leading to the formation of polypyrrole in the sponge network and resulting good conductivity of the sponge.

Preparation of active materials containing functional ink. At first, 1 g PU was ultrasonicated for 1h to dissolve in 8 mL NMP. Secondly, 81 mg conductive materials of Ketjen Black and 189 mg electrocatalysts (Pt@Au_{to}/rGO, N-C_{net}, $NiCo_2O_4$ and AC) were added into 1 mL PU/NMP solution with mass ration of 7: 3. The mixture was then ultrasonicated for 30 min and stirred for 24 h to obtain a screen printable uniform black color ink.

Fabrication of free-standing EFC and SC. The interdigitated shaped pattern of SC was designed by AutoCAD software. During screen-printing process, stretchable copper ink was firstly printed on 50% pre-stretching silicone rubber (4:1 mixture of part A and B) as current collector using 80 µm thick polyester stencil and dried at 60 °C for 5 min. The second layer of functional ink with $NiCo_2O_4$ materials was printed on left top of copper electrodes as positive electrode in SC. Another functional ink, consisting of AC electrocatalyst was printed on right top of copper electrodes as negative electrode in SC. Then electrodes were immersed into a chamber with deionized water (room temperature: 25 °C) for 10 min. To facilitate detachment of electrode film from substrate, 1 mm thickness of KOH-PVA hydrogel was covered on interdigitated shaped electrodes as both electrolyte and adhesive layer. Finally, silicone rubber substrate was released without stretching, and then fabricated SC was carefully peeled off from substrate to obtain flexible, interdigitated shaped electrodes with free standing interconnects.

The fabrication of EFC was same as process of SC with Pt@Au_{to}/rGO and N-C_{net} mixing in functional ink as electrocatalysts for EOR and ORR, respectively.

Fabrication of self-charging and self-powering Integrated system. The fabricated free-standing SC and EFC could be transferred to band aid substrate with KOH-PVA as both electrolyte and adhesive layer. In order to build integrated device, SC was integrated with EFC on one side of band aid; meanwhile, a motion sensor was attached on the other side, connected with energy harvesting/storge system in series. During sensing process, motion sensor was sticked on skin of tester; while EFC and SC were exposed to air, providing enough free space for ethanol spray

Characterization. Morphologies of Pt@Au_{to}/rGO, N-C_{net} and $NiCo_2O_4$ samples were observed by field emission scanning electron microscopy (FE-SEM, Carl Zeiss Ultra Plus, Germany) at an acceleration voltage of 5 kV. Transmission electron microscopy (TEM, Philips Tecnai G2F20) was used to study microstructure and composition of active NPs. Powder X-ray diffraction measurement (XRD, Rigaku D/MAX-2400 diffractometer) was used to confirm atomic constituents and crystal structures of Pt@Au_{to}/rGO and $NiCo_2O_4$ catalysts. The composition of Pt@Au_{to}/rGO and $NiCo_2O_4$ NPs was examined using X-ray photoelectron spectroscopy (XPS, PHI 550 apparatus).

Electrochemical Measurements. Electrochemical performance of Pt@Au_{to}/rGO NPs for EOR was firstly studied by CV curves in a standard three electrode system of 1.0 M KOH solution at room temperature. After pre-polished and cleaned glassy carbon electrode (0.7 cm^2), 4 µL catalyst ink was deposited on it as working electrode. Ag/AgCl and platinum wire were used as reference and counter electrode, respectively.

Linear sweep voltammetry (LSV) technologies were performed to study electrochemical performance of EFC. Output voltage (OCV) was carried out to study electrochemical sensing characteristic of EFC. All measurements were studied by a CHI 1242C Electrochemical workstation (Shanghai Chenhua instrument Co., Ltd., China). Capacitance performance of SC was studied by CV and galvanostatic charge/discharge (GCD) by CHI 660E (Shanghai Chenghua instrument Co., Ltd., China). CVs were test at different scan rates of 25, 50, 100, 150, 200 and 250 mV s^{-1}. GCDs were measured at current density of 0.5, 0.8, 1.0, 1.5 and 2 A g^{-1}. The performance of motion sensor was studied by i-t curves through CHI 1242C.

The specific capacitance (C_{sp}) was measured in terms of weight (F g^{-1}) and area (mF cm^{-2}) by Eq. S1 from its GCD curves:[5]

$$C_{sp} = \frac{I\Delta t}{x(V - IR_{drop})}$$

Here *x* is either mass of electrode (0.006 g) or the area (1 cm^2) of the device, *V* is the potential window, *I* is applied discharge current, *Δt* is discharge time.

The energy density (*E*) and power density (*P*) with respect to weight and area were measured by using Eq. S2 and Eq. S3, respectively:[5]

$$E = 0.5C_{sp}(V - IR_{drop})^2 \quad (S2)$$

$$P = \frac{E}{\Delta t} \quad (S3)$$

The mass loading of AC was determined by balancing the charges stored in each electrode as shown in Eq. S4:

$$C_{m+}V_{+}m_{+} = C_{m-}V_{-}m_{-}$$

Where m_+ and m_- are the mass loading of $NiCo_2O_4$ and AC in the free-standing electrode, C_{m+} and C_{m-} represent the specific capacitance of positive electrode (F g^{-1}) and negative electrode (F g^{-1}) respectively. *V* is the potential window of positive (+) and negative (-) electrode.

The resistance change (*ΔR*) of motion sensor was calculated as follows:

$$\Delta R = R_g - R_0 = \frac{V}{I_g - I_0}$$

Where R_0 and R_g is resistance of the sensor before and after applying of extra strain. I_0 and I_g are real-time current of the sensor before or after applying of extra strain, respectively.

2. Characterization of the free-standing electrode.

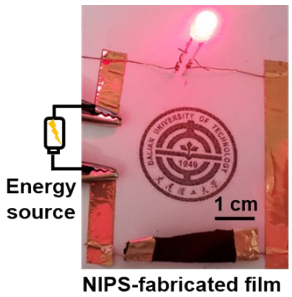

Fig. S1 Free-standing film obtained by NIPS as a conductive wire for lighting a red LED.

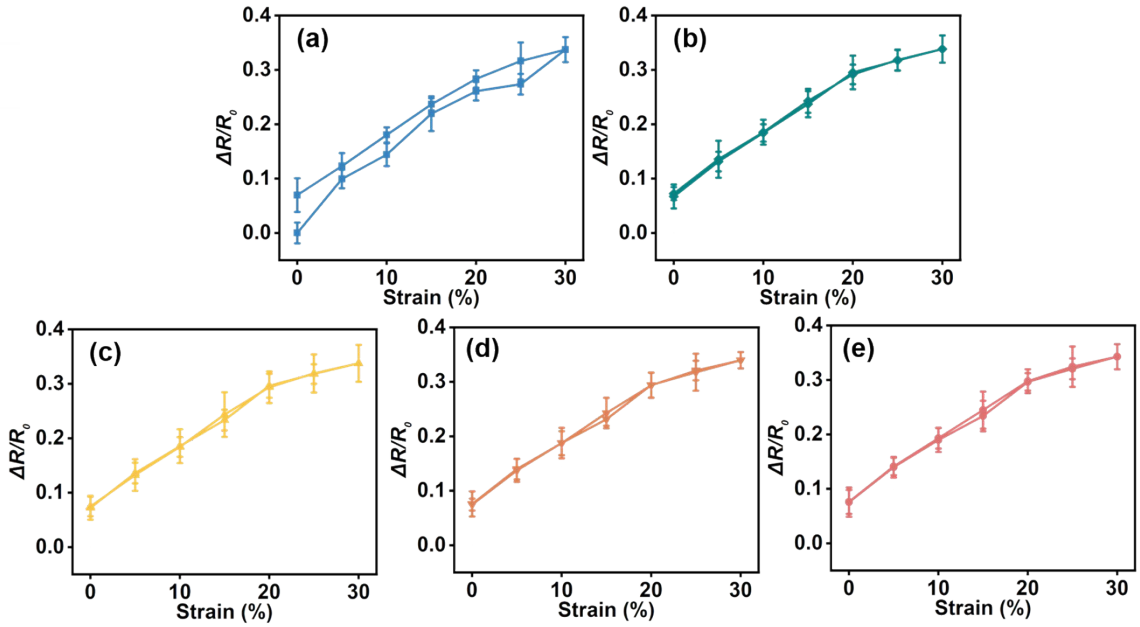

Fig. S2 Relative resistance changes as a function of tensile strain for the electrode at the (a) first, (b) second, (c) third, (d) forth, and (e) fifth cycle of stretching and releasing.

3. Characterization of the catalysts for EOR and ORR.

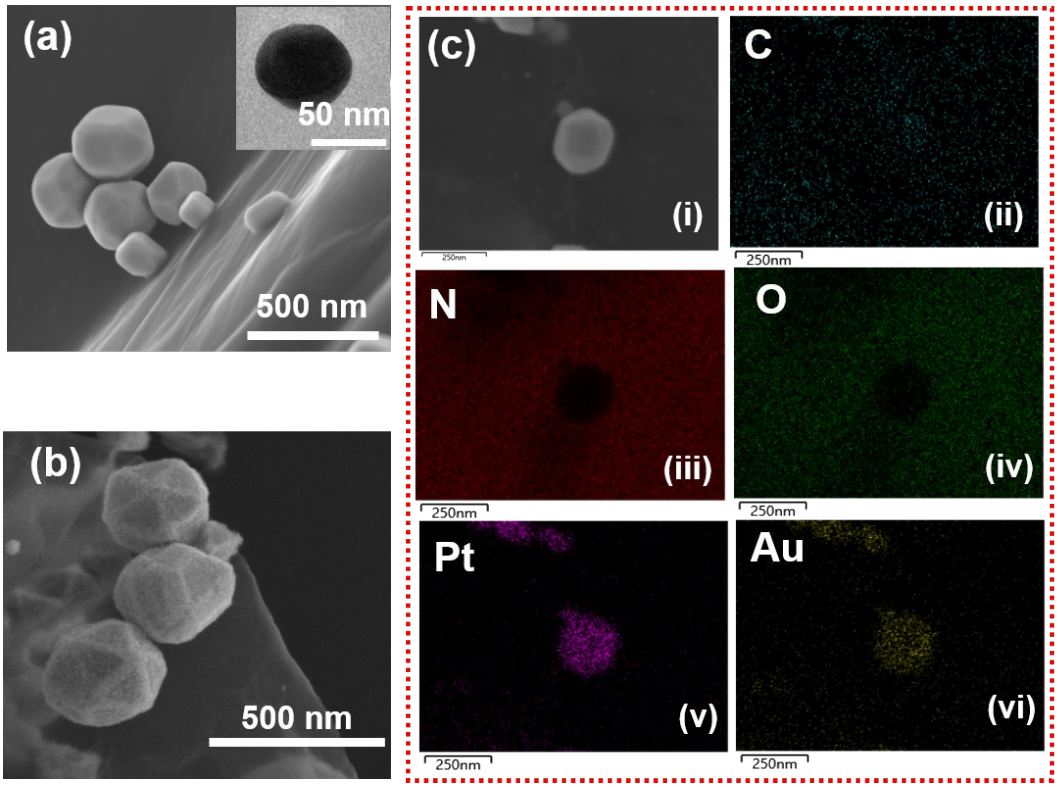

Fig. S3 Characterization of EOR catalyst. TEM image of (a) Au/rGO NPs, (b) Pt@Au_{to}/rGO NPs. (c) EDS mappings of Pt@Au_{to}/rGO, C, N, O, Pt, and Au, respectively.

Nanostructure and characterization of EOR catalysts were studied by SEM and TEM (Fig. S3). There showed thermodynamically stable and uniform truncated octahedron nanostructure of AuNPs modified on crumpled rGO, which were rapid reduction of Au precursor in high reaction temperature (200 °C).[6] Specific nanostructure of AuNPs was achieved by 1,5-pentanediol (PD) reductant and poly(vinyl pyrrolidone) (PVP) surface regulating polymer for reducing Au(III) to Au(I) and Au(0).[7-8] Meanwhile, $AgNO_3$ was introduced to promote the formation of truncated octahedron nanostructure AuNPs, and residual Ag^+ preferred to adsorb on Au (100) surfaces,[9-11] providing additional electrons for Pt^{2+} reduction.[10-12] As a result, PtNPs growth mainly occurred at vertices of Au truncated octahedra, which was further confirmed by EDS mapping, with Au existed in interior as core and Pt mainly in exterior as shell (Fig. S3c v, vi).

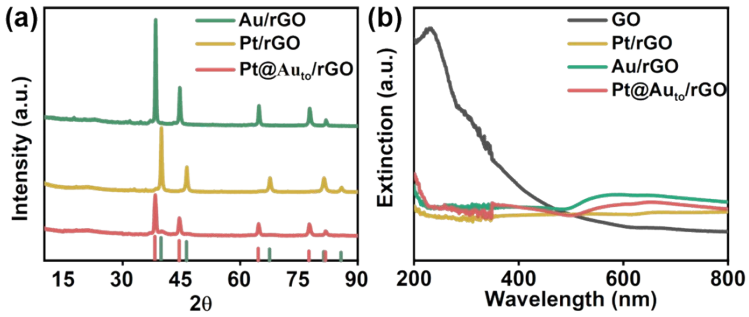

Fig. S4. Characterization of EOR catalyst. (a) XRD spectra of GO, Pt/rGO, Au/rGO and Pt@Au_{to}/rGO. (b) UV-vis spectra of Au/rGO, Pt/rGO and Pt@Au_{to}/rGO.

XRD patterns of Pt@Au_{to}/rGO NPs were studied (Fig. S4a). Peaks at 38.4, 44.6, 64.8 and 77.8°, corresponding to (111), (200), (220) and (311) diffraction planes of Au,[13] were clearly recognized both in Au/rGO and Pt@Au_{to}/rGO, indicating successfully deposition of AuNPs onto rGO nanosheets. There also appeared diffraction peaks of Pt (111), (200) and (220) occurred at 39.8, 46.5 and 67.65°; as well as rGO (002) observed at 22.85° as a broad and weak peak from Pt@Au_{to}/rGO. Well-shaped peaks of Pt and Au without syncretic suggested good crystalline phase separation of two metals in Pt@Au_{to}/rGO.[14] Characterization of Pt@Au_{to}/rGO was also verified by UV-Vis spectra (Figure S4b). Two absorption peaks of GO at 231.4 and 301.0 nm, were according to π-π* transition in aromatic C=C bond and n-π* transition in C=O bond, respectively.[15] When GO was reduced into rGO, original electronic conjugation was restored, resulting into disappearance of two peaks and present of a broad peak at 250 nm from rGO. A broad peak appeared between 490 to 660 nm after introduction of AuNPs; while the peak dramatic broadened after formation of Pt shell.[16] Meanwhile, shorter chemical bonds between Pt@Au_{to} NPs and rGO greatly changed localized electromagnetic field for faster electron transfer,[17-18] making slightly redshift of broad peak.

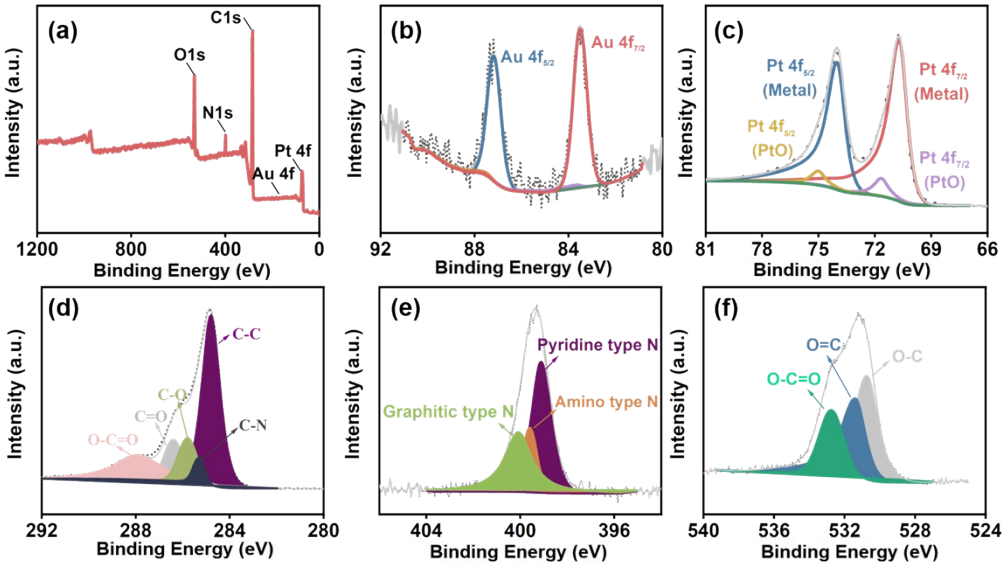

Fig. S5. XPS spectrum of (a) Pt@Au_{to}/rGO; Core level spectra of (b) Au 4f; (c) Pt 4f; (d) C1s; (e) N1s; (f) O1s.

Furthermore, binding energies of Pt 4f ($4f_{7/2}$ = 70.70 eV, $4f_{5/2}$ = 74.03 eV) and Au 4f ($4f_{7/2}$ = 83.48 eV, $4f_{5/2}$ = 87.21 eV) peaks in high-resolution XPS spectrum (Fig. S5b,c) indicated existence of Pt^0 and Au^0 atoms in Pt@Au_{to}/rGO. Binding energies to carbon functional groups of C-C (284.8 eV), C-N (285.29 eV), C-O (285.8 eV), C=O (286.4 eV) and O-C=O (288.02 eV) were also measured from C1s XPS (Fig. S5d).[19] From N1s XPS spectrum (Figure S5e), three nitrogen functional groups of pyridinic-type N (397.7 eV), amino-type N (399.53 eV) and graphitic-type N (400.9 eV) were observed.[20] O1s XPS spectra (Fig. S5f) showed deconvolution yielded three constituents of O–C (530.7 eV), O=C (531.4 eV) and O–C=O (532.7 eV).[21]

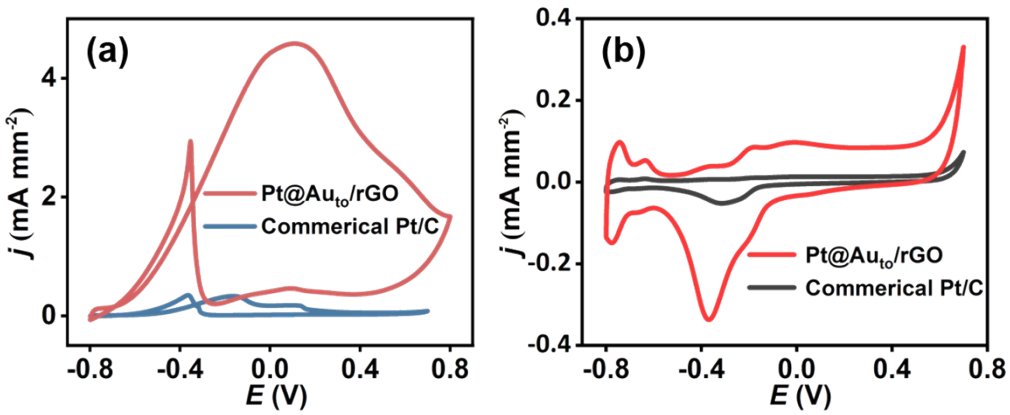

Fig. S6. CV comparison of commercial 10% Pt/C and Pt@Au_{to}/rGO catalysts on glassy carbon electrode in (a) 1.0 M KOH consisting of 1.0 M ethanol (100 mV s^{-1}); (b) N_2-saturated with 1.0 M KOH (50 mV s^{-1}).

CV curves were used to study electrocatalytic performance of Pt@Au_{to}/rGO (Fig. S6a). During forward oxidation peak of EOR, CO_2, acetic acid and acetaldehyde were main oxidation products towards -0.6-0.6 V through C_1 or C_2 pathway (Fig. S6).[22] While backward oxidation peak at -0.35 V was contributed to oxidation process of partial oxidation intermediates such as CO_{ads}. Two obviously oxidation peaks indicated excellent electrocatalytic properties of Pt@Au_{to}/rGO, compared with commercial 10% Pt/C or Au/rGO materials. Moreover, higher electrochemically active surface area (ECSA) of Pt@Au_{to}/rGO than commercial 10% Pt/C or Au/rGO has received from hydrogen adsorption-desorption peak (Fig. S6b),[23] suggesting more free surface-active sites for electrocatalysis.[24]

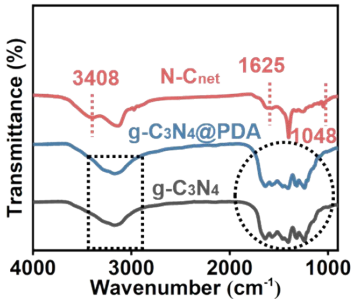

Fig. S7. FTIR spectra of g-C_3N_4, g-C_3N_4@PDA and N-C_{net}.

As shown in Fig. S7, FTIR peaks between 1073-1774 cm^{-1} and 2924-3300 cm^{-1} in g- C_3N_4 or g- C_3N_4@PDA belonged to N-C heterocycles and N-H group stretching vibration, respectively (Fig. S7).[3] O-H, N-H or other chemical bonds were destroyed during high-temperature carbonization, resulting only remained three peaks at 1048, 1625 and 3408 cm^{-1} in N-C_{net}, contributing to C-C and C-N vibration, respectively.[3] Moreover, remained C-N bond was stable, ensuring effective doping of nitrogen element.

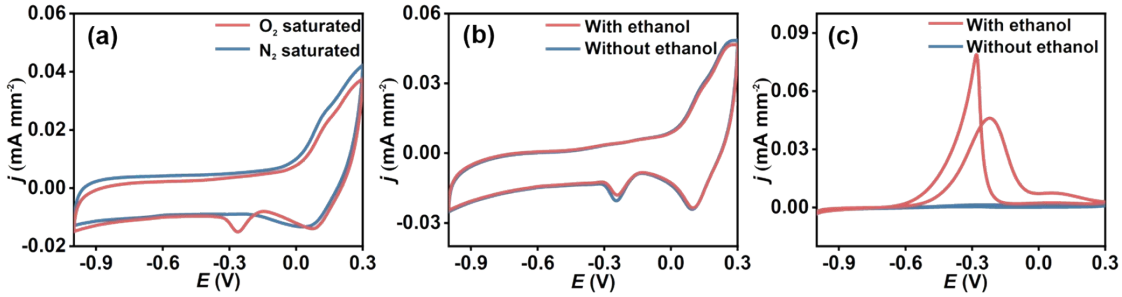

Fig. S8. Electrochemical performance of N-C_{net} catalyst. CV curves of N-C_{net} catalyst under (a) O_2 or N_2 saturated vapor (10 mV s^{-1}) in 1 M KOH; (b) O_2 saturated vapor with (red curve) and without (blue curve) 20% ethanol (10 mV s^{-1}) in 1 M KOH. (c) CV curves of commercial 10% Pt/C catalyst under O_2 saturated vapor with (red curve) and without (blue curve) 20% ethanol (10 mV s^{-1}) in 1 M KOH.

An obvious oxygen reduction peak at -0.26 V was observed from N-C_{net} catalyst (Fig. S8a), indicating good catalytic behavior of cathode for ORR. Additionally, N-C_{net} catalyst showed excellent tolerance of ethanol compared with commercial 10% Pt/C with apparent oxidation peak under ethanol (Fig. S8b, c), which was consistent with previous report.[25]

4. Electrochemical performance of ethanol fuel cell (EFC)

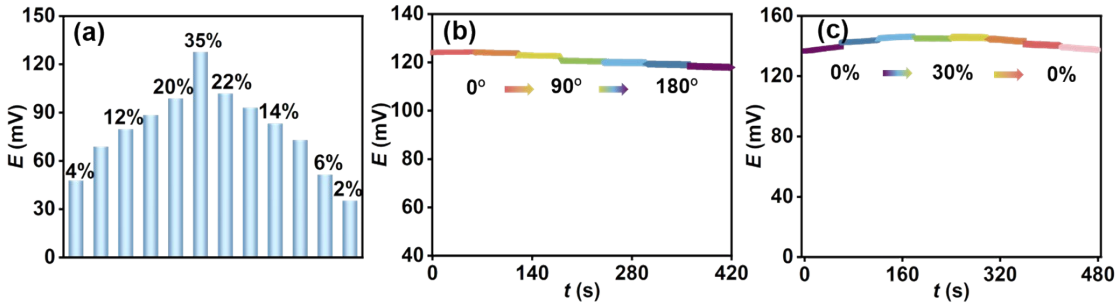

Fig. S9. Electrochemical performance of free-standing Pt@Au_{to}/rGO//N-C_{net} EFC. (a) Real-time OCV of EFC varying ethanol spray concentration. Discharge behaviors under (b) bending (0-180° at an increment of 20°); (c) stretching (5-30% at an increment of 5%) under 35% ethanol spray.

5. Characterization of $NiCo_2O_4$

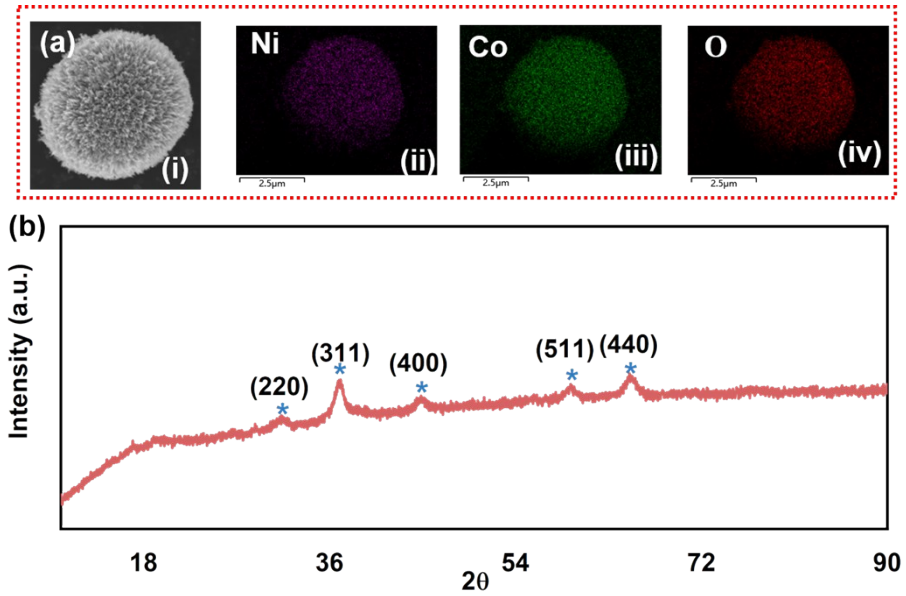

Fig. S10. (a) EDS mappings of $NiCo_2O_4$, Ni, Co and O respectively. (b) XRD spectra of $NiCo_2O_4$.

Uniformly distribution of Ni, Co and O element on NPs was confirmed by EDS mapping with purple, green and red color, respectively (Fig. S10a). XRD spectra further indicated crystal structures of as-prepared $NiCo_2O_4$ (Fig. S10b). Diffraction peaks at 31.39, 37.08, 44.98, 59.33 and 65.14° were corresponding to $NiCo_2O_4$ (220), (311), (400), (511) and (440).[26-27]

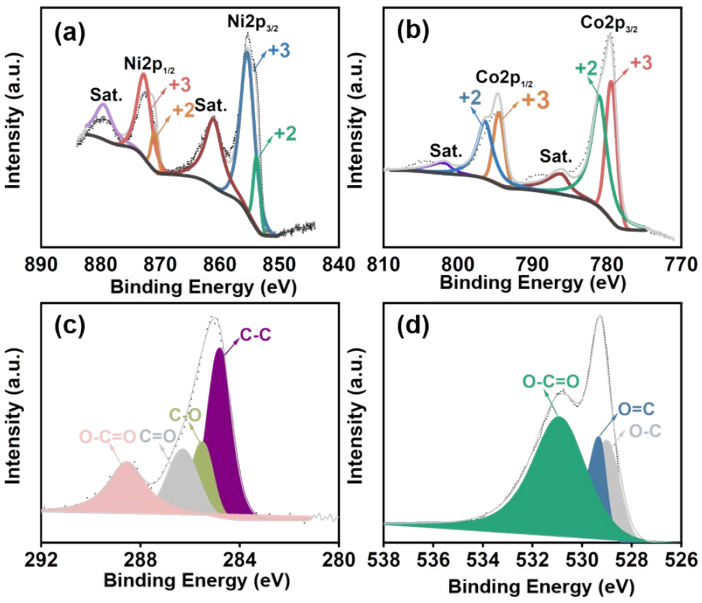

Fig. 11. XPS spectra of (a) Ni 2p; (b) Co 2p; (c) C1s; (d) O1s from $NiCo_2O_4$.

XPS was carried out to character detailed electronic states of $NiCo_2O_4$ nanosheets. Two spin-orbit doublets characteristic of Ni^{2+} and Ni^{3+}, as well as two shake-up satellite peaks were observed in high-resolution Ni 2p spectrum (Fig. S11a). Binding peaks at 853.8 and 870.9 eV were according to Ni^{2+}, while peaks at 855.4 and 872.72 eV could be attributed to Ni3+4. Similarly, binding peaks at 779.42 and 794.47 eV could be indexed to Co^{3+} (Fig. S11b).[4] Meanwhile, C 1s spectrum was also studied with four peaks at 284.79, 285.5, 286.3, and 288.1 eV (Fig. S11c), assigning to C-C, C-O, C=O, and O-C=O bonds, respectively.[4] Similarly, deconvolution peaks of O 1s spectrum were resolved into three components as 529.02, 529.31 and 530.9 eV (Fig. S11d), which was attributed to O-C, O=C and O-C=O.[4]

6. Electrochemical performances of $NiCo_2O_4$-based SC

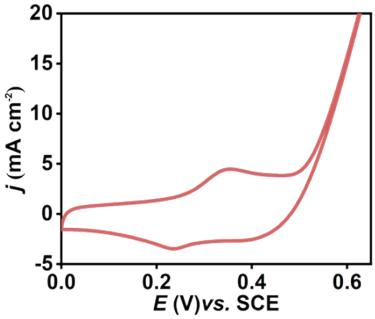

Fig. S12. CV analysis of $NiCo_2O_4$ in three electrode system at 1 mV s^{-1}.

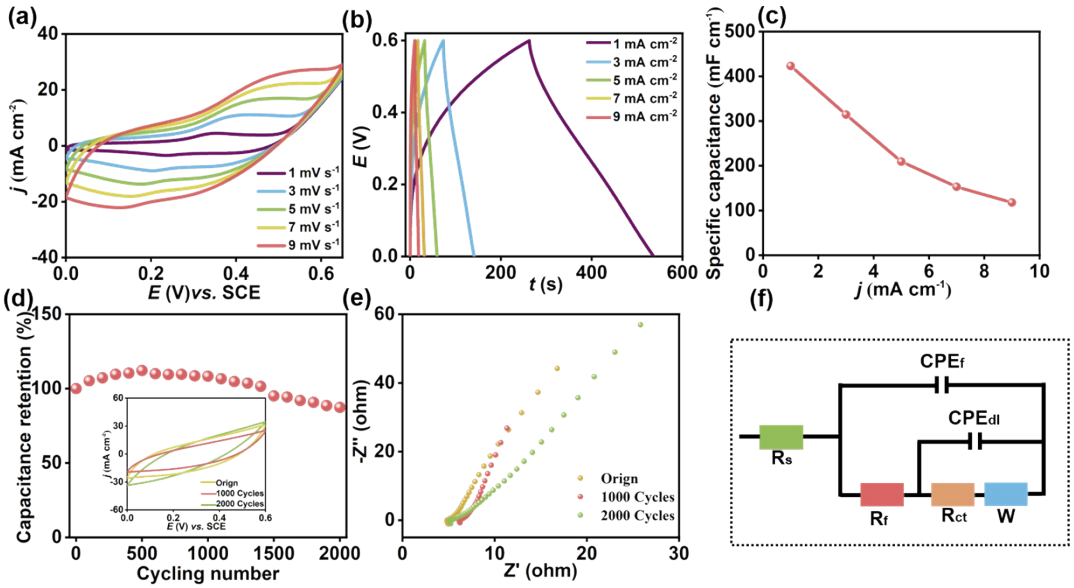

Fig. S13. Electrochemical behaviors of $NiCo_2O_4$ in three electrode system. (a) CV analysis of the SC at different scan rates. (b) GCD of the SC at different current densities. (c) Variation of specific capacitance for different current densities. (d) Cycling performance of the SC at 100 mV s^{-1}. Inset: CV curves of 0, 1000 or 2000 cycles, respectively. (e) Nyquist plots of $NiCo_2O_4$ electrode of 0, 1000, and 2000 cycling cycles at open circuit potential. (f) The equivalent circuit for modeling Nyquist plots.

The specific capacitance remained around 85% of the initial value after 2000 cycles (Fig. S13d), as well as stable curves by CV and electrochemical impedance spectroscopy (EIS) (Fig. S13d and e). The good stability of the SC indicated homogenous and stable dispersion of active materials in the NIPS-fabricated free-standing electrode. Furthermore, the equivalent circuit for modelling Nyquist plots showed equivalent series resistance (R_S) in the X-axis intercept of high frequency,[28] consisting of ionic resistance, electronic resistance and interface resistance (Fig. S13f). The small value of R_S, as well as the steeply straight line in the low frequency region, indicated the high conductivity of the free-standing electrode via NIPS.

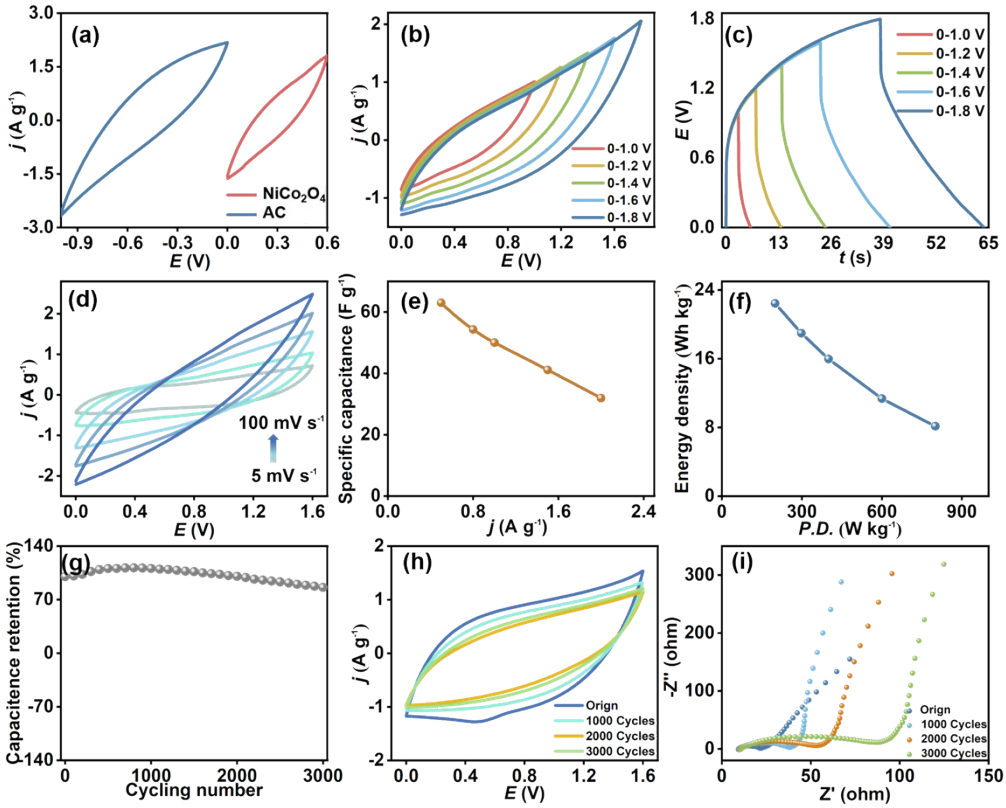

Fig. S14. Electrochemical behaviors of $NiCo_2O_4$//AC SC. (a) CV curves of $NiCo_2O_4$ and AC half cells in 1 M KOH solution at a scan rate of 100 mV s^{-1}. (b) CV curves (100 mV s^{-1}) and (c) GCD curves (2 A g^{-1}) of prepared SCs under different potential window. (d) CV at different scan rate with a potential window of 0-1.6 V. (e) Variation of specific capacitance for different current densities. (f) Ragone plot of as-obtained SC. (g) Cycling performance of the SC at 100 mV s^{-1}. (h) CV curves of 0, 1000, 2000 and 3000 cycling cycles. (i) Nyquist plots of SC for 0, 1000, 2000 and 3000 cycling cycles at open circuit potential.

At first, different potential windows (1.0, 1.2, 1.4, 1.6 and 1.8 V) were carried out by CVs (Fig. S14b). A distinct polarization was observed with potential of up to 1.8 V due to the voltage drop (IR_{drop}) of the SC. Furthermore, the stable capacitance performance of the device was in a potential window as high as 1.6 V. Meanwhile, the dependence of GCD on the potential window (1.0, 1.2, 1.4, 1.6 and 1.8 V) further confirmed the above results (Fig. S14c). The symmetrical non-ideal triangular shapes in the GCD curves suggested the reversibility of the SC during the charging/discharging process in a wide potential window.[29] However, IR_{drop} increased with increasing applied potential with 30 and 44.4 mV for 0–1.6 and 0–1.8 V, respectively.

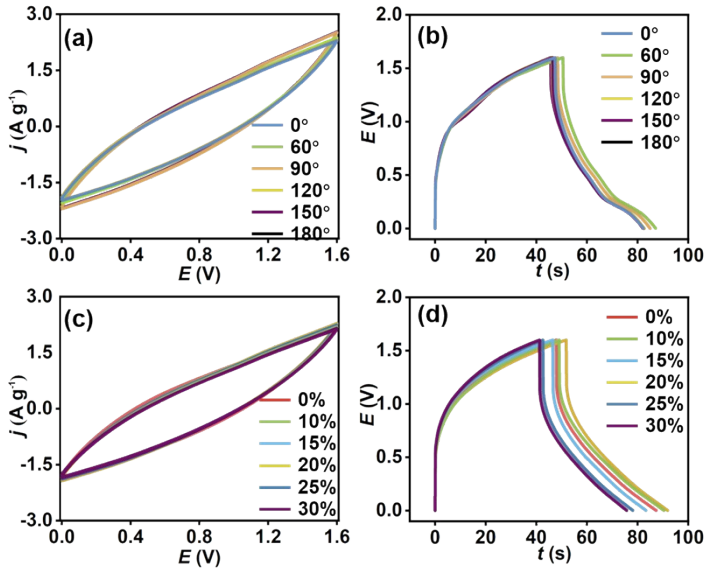

Fig. S15. Electrochemical behaviors of $NiCo_2O_4$//AC SC. Electrochemical performance of SC under different bending angles (a) CV curves (100 mV s^{-1}) and (b) GCD curves (2 A g^{-1}). Electrochemical performance of SC under different stretching precents (c) CV curves (100 mV s^{-1}) and (d) GCD curves (2 A g^{-1}).

References

[1] H. Ma, Y. Jiang, J. Ma, X. Ma, M. Xue, N. Zhu, *Anal Chem* **2020**, 92, 5897.
[2] M. Min, C. Kim, Y. I. Yang, J. Yi, H. Lee, *Phys Chem Chem Phys* **2009**, 11, 9759.
[3] C. Li, X. Li, X. Sun, X. Zhang, L. Duan, X. Yang, L. Wang, W. Lu, *Nanoscale Res Lett* **2019**, 14, 249.
[4] M. Yan, Y. Yao, J. Wen, L. Long, M. Kong, G. Zhang, X. Liao, G. Yin, Z. Huang, *ACS Appl Mater Interfaces* **2016**, 8, 24525.
[5] H. Ma, F. Lv, L. Shen, K. Yang, Y. Jiang, J. Ma, X. Geng, T. Sun, Y. Pan, Z. Xie, M. Xue, N. Zhu, *Energy & Environmental Materials* **2021**, DOI: 10.1002/eem2.12227.
[6] T. K. Sau, C. J. Murphy, *J Am Chem Soc* **2004**, 126, 8648.
[7] B. Wiley, Y. Sun, J. Chen, H. Cang, Z.-Y. Li, X. Li, Y. Xia, *MRS Bulletin* **2011**, 30, 356. [8] Y. Sun, Y. Yin, B. T. Mayers, T. Herricks, Y. Xia, *Chemistry of Materials* **2002**, 14, 4736.
[9] D. Seo, J. C. Park, H. Song, *J Am Chem Soc* **2006**, 128, 14863.
[10] J. Pérez-Juste, L. M. Liz-Marzán, S. Carnie, D. Y. C. Chan, P. Mulvaney, *Advanced Functional Materials* **2004**, 14, 571.
[11] J. H. Song, F. Kim, D. Kim, P. Yang, *Chemistry* **2005**, 11, 910.
[12] L. Feng, X. Wu, L. Ren, Y. Xiang, W. He, K. Zhang, W. Zhou, S. Xie, *Chemistry* **2008**, 14, 9764.
[13] S. Zhang, Y. Shao, H.-g. Liao, J. Liu, I. A. Aksay, G. Yin, Y. Lin, *Chemistry of Materials* **2011**, 23, 1079.
[14] G. Yang, Y. Li, R. K. Rana, J.-J. Zhu, *J. Mater. Chem. A* **2013**, 1, 1754.
[15] J. Shang, L. Ma, J. Li, W. Ai, T. Yu, G. G. Gurzadyan, *Sci Rep* **2012**, 2, 792.
[16] S. G. Jang, A. Khan, M. D. Dimitriou, B. J. Kim, N. A. Lynd, E. J. Kramer, C. J. Hawker, *Soft Matter* **2011**, 7.
[17] R. K. Biroju, B. Choudhury, P. K. Giri, *Catalysis Science & Technology* **2016**, 6, 7101.
[18] Q. Chi, J. Zhang, J. E. T. Andersen, J. Ulstrup, *The Journal of Physical Chemistry B* **2001**, 105, 4669.
[19] K. R. Lee, K. U. Lee, J. W. Lee, B. T. Ahn, S. I. Woo, *Electrochemistry Communications* **2010**, 12, 1052.
[20] L. S. Zhang, X. Q. Liang, W. G. Song, Z. Y. Wu, *Phys Chem Chem Phys* **2010**, 12, 12055.
[21] P. Bera, K. R. Priolkar, A. Gayen, P. R. Sarode, M. S. Hegde, S. Emura, R. Kumashiro, V. Jayaram, G. N. Subbanna, *Chemistry of Materials* **2003**, 15, 2049.
[22] Z. X. Liang, T. S. Zhao, J. B. Xu, L. D. Zhu, *Electrochimica Acta* **2009**, 54, 2203.
[23] J. Chang, L. Feng, K. Jiang, H. Xue, W.-B. Cai, C. Liu, W. Xing, *Journal of Materials Chemistry A* **2016**, 4, 18607.
[24] Y. Lu, Y. Jiang, W. Chen, *Nanoscale* **2014**, 6, 3309.
[25] H. Ma, Q. Liu, P. Cheng, L. Shen, J. Ma, F. Lv, Y. Zhang, Y. Jiang, T. Sun, N. Zhu, *ACS Sens* **2021**, 6, 4526.
[26] W.-w. Liu, C. Lu, K. Liang, B. K. Tay, *J. Mater. Chem. A* **2014**, 2, 5100.
[27] J. Du, G. Zhou, H. Zhang, C. Cheng, J. Ma, W. Wei, L. Chen, T. Wang, *ACS Appl Mater Interfaces* **2013**, 5, 7405.
[28] Rajendran V., Mohan A. M. V., Jayaraman M., Nakagawa T., *Nano Energy* **2019**, 65, 104055.
[29] Ma H., Lv F., Shen L., Yang K., Jiang Y., Ma J., Geng X., Sun T., Pan Y., Xie Z., Xue M., Zhu N., *Energy Environ. Mater.* **2021** 1-10